

What are we learning from the relative orientation between density structures and the magnetic field in molecular clouds?

J. D. Soler¹ and P. Hennebelle²

¹ Max-Planck-Institute for Astronomy, Königstuhl 17, 69117 Heidelberg, Germany
e-mail: soler@mpia.de

² Laboratoire AIM, Paris-Saclay, CEA/IRFU/SAP – CNRS – Université Paris Diderot, 91191 Gif-sur-Yvette Cedex, France

Received 26 April 2017 / Accepted 4 September 2017

ABSTRACT

We investigate the conditions of ideal magnetohydrodynamic (MHD) turbulence responsible for the relative orientation between density gradients ($\nabla\rho$) and magnetic fields (\mathbf{B}) in molecular clouds (MCs). For that purpose, we construct an expression for the time evolution of the angle (ϕ) between $\nabla\rho$ and \mathbf{B} based on the transport equations of MHD turbulence. Using this expression, we find that the configuration where $\nabla\rho$ and \mathbf{B} are mostly parallel, $\cos\phi = \pm 1$, and where $\nabla\rho$ and \mathbf{B} are mostly perpendicular, $\cos\phi = 0$, constitute equilibrium points, that is, the system tends to evolve towards either of these configurations and they are more represented than others. This would explain the predominant alignment or anti-alignment between column density (N_{H}) structures and the projected magnetic field orientation ($\langle\hat{\mathbf{B}}_{\perp}\rangle$) reported in observations. Additionally, we find that departures from the $\cos\phi = 0$ configurations are related to convergent flows, quantified by the divergence of the velocity field ($\nabla\cdot\mathbf{v}$) in the presence of a relatively strong magnetic field. This would explain the observed change in relative orientation between N_{H} structures and $\langle\hat{\mathbf{B}}_{\perp}\rangle$ towards MCs, from mostly parallel at low N_{H} to mostly perpendicular at the highest N_{H} , as the result of the gravitational collapse and/or convergence of flows. Finally, we show that the density threshold that marks the observed change in relative orientation towards MCs, from N_{H} and $\langle\hat{\mathbf{B}}_{\perp}\rangle$ being mostly parallel at low N_{H} to mostly perpendicular at the highest N_{H} , is related to the magnetic field strength and constitutes a crucial piece of information for determining the role of the magnetic field in the dynamics of MCs.

Key words. magnetohydrodynamics (MHD) – turbulence – ISM: general – ISM: structure – ISM: magnetic fields – ISM: clouds

1. Introduction

The advent of novel observations of polarization from dust, in emission at submillimeter wavelengths and in absorption from background stars in the visible and near-infrared, provides an unprecedented amount of information on the magnetic field orientation integrated along the line of sight and projected on the plane of the sky ($\langle\hat{\mathbf{B}}_{\perp}\rangle$) at molecular cloud (MC) scales (Crutcher 2012; Planck Collaboration I 2016). However, integrating this information to our understanding of the dynamical processes that produce density structures in the interstellar medium (ISM), from MCs to filaments and eventually stars, remains challenging (Bergin & Tafalla 2007; Hennebelle & Falgarone 2012; Klessen & Glover 2016).

One simple approach to obtain insight into the role of the magnetic field is the study of the relative orientation between the observed column density (N_{H}) structures and $\langle\hat{\mathbf{B}}_{\perp}\rangle$. Multiple studies of $\langle\hat{\mathbf{B}}_{\perp}\rangle$ inferred from starlight polarization (e.g., Palmeirim et al. 2013; Li et al. 2013; Sugitani et al. 2011 and more recently Kusune et al. 2016; Santos et al. 2016; Soler et al. 2016; Hoq et al. 2017) use qualitative descriptions of the relative orientation between $\langle\hat{\mathbf{B}}_{\perp}\rangle$ and the N_{H} structures to argue the importance of the magnetic field in structuring the observed regions.

In emission from the diffuse ISM, quantitative analysis of the polarization observations at 353 GHz by the ESA *Planck* satellite show that over most of the sky, the majority of the elongated N_{H} structures traced by dust thermal emission are predominantly aligned with the magnetic field measured on the

structures (Planck Collaboration Int. XXXII 2016). This statistical trend, which becomes less striking with increasing column density, is similar to that found between low column density ($N_{\text{H}} \approx 5 \times 10^{18} \text{ cm}^{-2}$) fibers traced by HI emission and $\langle\hat{\mathbf{B}}_{\perp}\rangle$ (Clark et al. 2014; Kalberla et al. 2016).

In emission from the denser ISM, quantitative analysis of the *Planck* polarization observations at 353 GHz towards ten nearby ($d < 450 \text{ pc}$) MCs shows that the relative orientation between the column density structures and $\langle\hat{\mathbf{B}}_{\perp}\rangle$ progressively changes with increasing column density from mostly parallel at $\log(N_{\text{H}}/\text{cm}^{-2}) \lesssim 21.7$ to mostly perpendicular at $\log(N_{\text{H}}/\text{cm}^{-2}) \gtrsim 21.7$ (Planck Collaboration Int. XXXV 2016). Subsequent studies of the relative orientation between N_{H} structures and $\langle\hat{\mathbf{B}}_{\perp}\rangle$ have identified similar trends using N_{H} structures derived from *Herschel* observations at 20'' resolution and $\langle\hat{\mathbf{B}}_{\perp}\rangle$ inferred from BLASTPol polarization observation at 250, 350, and 500 μm towards the Vela C molecular complex (Soler et al. 2017) as well as using N_{H} structures derived from *Herschel* observations together with *Planck* 353 GHz polarization observations towards the high-latitude cloud L1642 (Malinen et al. 2016).

From the theoretical point of view, the magnetic field (\mathbf{B}), whose observed energy density is in rough equipartition with other energy densities in the local ISM (Heiles & Crutcher 2005), imposes an asymmetry for the formation of condensations from the diffuse ISM. Condensation modes are unaffected when they propagate parallel to the mean direction of the field (\mathbf{B}_0), but inhibited by the magnetic pressure when they propagate

normal to \mathbf{B}_0 (Field 1965). Consequently, condensations driven by thermal instability arise along \mathbf{B}_0 and MCs can be formed by shock waves only if the perturbations propagate almost parallel to the mean magnetic field (Hennebelle & Pérault 2000; Hartmann et al. 2001; Inoue et al. 2007; Körtgen & Banerjee 2015).

This theoretical framework suggests that the observed regimes in relative orientation between N_H structures and $\langle \hat{\mathbf{B}}_{\perp} \rangle$ indicate something fundamental about the gathering of gas out of the diffuse ISM, which results in the formation of MCs and their subsequent evolution to form denser structures, such as filaments and cores. In this work, we explore the relation between the observed relative orientation between $\langle \hat{\mathbf{B}}_{\perp} \rangle$ and the N_H structures and the conditions imposed by the transport equations of magnetohydrodynamic (MHD) turbulence. For that purpose, we construct an expression for the evolution of the relative orientation between $\nabla\rho$ and \mathbf{B} and evaluate the physical processes that are potentially responsible for the observed trends.

This paper is organized as follows. In Sect. 2 we introduce the transport equations of MHD turbulence and derive an expression for the relative orientation between $\nabla\rho$ and \mathbf{B} . In Sect. 3 we discuss the implications of the derived relation and characterize it using, first, a set of simple cases and, second, the simulations of MHD turbulence in MCs that were used to characterize the analysis method presented in Planck Collaboration Int. XXXV (2016). Section 4 discusses the implications of the studied relation between $\nabla\rho$ and \mathbf{B} . Finally, Sect. 5 gives our conclusions and anticipates future work. We reserve some additional analyses to Appendix A, where we present an expression for time evolution of the relative orientation between the magnetic fields, \mathbf{B} , and the velocity fields, \mathbf{v} .

2. Relative orientation between \mathbf{B} and iso-density contours

2.1. Transport equations of magnetohydrodynamic turbulence

Using the Lagrangian form of the equations, which corresponds to looking at the fluid motion following an individual parcel as it moves through space and time, the continuity equation, which guarantees the conservation of mass, is

$$\frac{d\log\rho}{dt} = -\partial_i v_i, \quad (1)$$

where ρ and v_i respectively are the density and velocity; the index i ranges between 0 and 2 and represents the axes of a 3D Cartesian reference frame. Here, and in the rest of the paper, summation over repeated indexes is implied following the Einstein summation convention.

The magnetic field \mathbf{B} is described by the Faraday equation

$$\nabla \times \mathbf{E} = -\partial_t \mathbf{B}, \quad (2)$$

where \mathbf{E} is the electric field. Under the assumption of low magnetic diffusivity, Eq. (2) reduces to

$$\partial_t \mathbf{B} = \nabla \times (\mathbf{v} \times \mathbf{B}), \quad (3)$$

which can be expanded as

$$\frac{dB_i}{dt} = B_j(\partial_j v_i) - B_i(\partial_j v_j). \quad (4)$$

2.2. Time evolution of the relative orientation between $\nabla\rho$ and \mathbf{B}

We construct an expression for the behavior of $\cos\phi$, the angle between $\nabla\rho$ and \mathbf{B} , by combining the equations introduced in Sect. 2.1 as follows. By the definition of the scalar product of vectors, the cosine of the angle between $\nabla\rho$ and \mathbf{B} corresponds to

$$\begin{aligned} \cos\phi &= \frac{\nabla\rho \cdot \mathbf{B}}{|\nabla\rho| |\mathbf{B}|} \\ &= \frac{R_i B_i}{(R_j R_j)^{1/2} (B_k B_k)^{1/2}}, \end{aligned} \quad (5)$$

where we introduce the convention $R_i \equiv \partial_i \log\rho$. We note that the distribution of relative orientations between two sets of uniformly distributed random vectors in 3D is flat in the cosine of their separation angle, thus all the discussions of relative orientations in 3D are given in terms of $\cos\phi$ (see Appendix C of Planck Collaboration Int. XXXV 2016).

We apply the time derivative to the square of Eq. (5) and, assuming that the spatial and time derivatives can be commuted, we obtain

$$\begin{aligned} \frac{d(\cos^2\phi)}{dt} &= \frac{2}{(R_k R_k)^2 (B_k B_k)^2} \left[\frac{d(R_i B_i)}{dt} (R_m R_m) (B_n B_n) \right. \\ &\quad \left. - \frac{d(B_i)}{dt} B_i (R_j B_j)^2 (R_m R_m) - \frac{d(R_i)}{dt} R_i (B_n B_n) (R_j B_j)^2 \right]. \end{aligned} \quad (6)$$

Using the definitions

$$r_i \equiv \frac{R_i}{(R_k R_k)^{1/2}}, \quad (7)$$

and

$$b_i \equiv \frac{B_i}{(B_k B_k)^{1/2}}, \quad (8)$$

which imply $\cos\phi = r_i b_i$, Eq. (6) becomes

$$\begin{aligned} \frac{d(\cos\phi)}{dt} &= \frac{1}{(R_k R_k)^{1/2} (B_k B_k)^{1/2}} \frac{d(R_i B_i)}{dt} \\ &\quad - \left[\frac{b_i}{(B_k B_k)^{1/2}} \frac{d(B_i)}{dt} + \frac{r_i}{(R_k R_k)^{1/2}} \frac{d(R_i)}{dt} \right] \cos\phi, \\ &= [r_i - b_i \cos\phi] \frac{1}{(B_k B_k)^{1/2}} \frac{d(B_i)}{dt} \\ &\quad + [b_i - r_i \cos\phi] \frac{1}{(R_k R_k)^{1/2}} \frac{d(R_i)}{dt}. \end{aligned} \quad (9)$$

This result is nothing but a generalization of $d(\cos\phi)/dt = -\sin\phi (d\phi/dt)$. If $d\phi/dt \neq 0$, then $d\cos\phi/dt = 0$ when $\cos\phi = \pm 1$.

In the particular case where $\cos\phi = \pm 1$, which corresponds to $r_i = \pm b_i$, Eq. (9) becomes $d(\cos\phi)/dt = 0$, thus implying that this configuration is an equilibrium point, that is, a configuration towards which the system tends to evolve for a wide variety of starting conditions. Potentially, this configuration is also an attractor, meaning that the system can remain in this configuration even if slightly disturbed. This equilibrium point is generic in the sense that it is purely geometrical and does not depend on the details of the physics, as long as the time derivatives in Eq. (9) do not become infinite when $\cos\phi = \pm 1$.

From Eq. (1) we get

$$\partial_i \left[\frac{d(\log \rho)}{dt} \right] = -\partial_i(\partial_j v_j), \quad (10)$$

which is equivalent to

$$\frac{d(R_i)}{dt} = -\partial_i(\partial_j v_j) - (\partial_i v_j) R_j. \quad (11)$$

Introducing Eqs. (4) and (11) into Eq. (9) we obtain

$$\frac{d(\cos \phi)}{dt} = \frac{\partial_i(\partial_j v_j)}{(R_k R_k)^{1/2}} [-b_i + r_i \cos \phi] + (\partial_i v_j)[r_i r_j - b_i b_j] \cos \phi, \quad (12)$$

which corresponds to the time evolution of the cosine of the angle between $\nabla \rho$ and \mathbf{B} . We note that this expression is entirely based on the transport equations of ideal MHD turbulence. It is composed of the strain tensor $\partial_i v_j$ (Landau et al. 1986), and the symmetric tensors $r_i r_j$ and $b_i b_j$, which represent the correlation of the density gradient orientation and the correlation between the components of the magnetic field orientation, respectively.

For the sake of simplicity, in the rest of this document we rewrite Eq. (12) as

$$\frac{d(\cos \phi)}{dt} = C + [A_1 + A_{23}] \cos \phi, \quad (13)$$

where we use the definitions

$$A_1 \equiv \frac{\partial_i(\partial_j v_j)}{(R_k R_k)^{1/2}} r_i, \quad (14)$$

$$C \equiv -\frac{\partial_i(\partial_j v_j)}{(R_k R_k)^{1/2}} b_i, \quad (15)$$

and

$$A_{23} \equiv (\partial_i v_j)[r_i r_j - b_i b_j], \quad (16)$$

which, without any loss in generality, can be expressed as

$$A_{23} \equiv \frac{1}{2}(\partial_i v_j + \partial_j v_i)[r_i r_j - b_i b_j]. \quad (17)$$

For the sake of comparison with previous works that studied the relative orientation between \mathbf{B} and \mathbf{v} (Matthaeus et al. 2008; Banerjee et al. 2009), we obtained a similar expression for the relative orientation between those two quantities and present it in Appendix A.

3. Interpretation

A few points can be readily concluded from Eq. (13). First, given that the coefficient C is on average very small (as will be shown in Sect. 3.2), $\cos \phi = 0$ constitutes another equilibrium point. This means that, under the assumptions presented in Sect. 2, we expect either $\cos \phi = \pm 1$ or $\cos \phi = 0$; that is, \mathbf{B} tends to be either parallel or perpendicular to the density structures. Second, the relative orientation between $\nabla \rho$ and \mathbf{B} changes by the effect of the coupling between the motions of the fluid represented by the strain tensor $\partial_i v_j$ and the symmetric unitary tensors $r_i r_j$ and $b_i b_j$. To better understand the implications of Eq. (13), we present the study of few simple cases in Sect. 3.1 and of a set of simulations of MHD turbulence in Sect. 3.2.

3.1. Study of simple cases

In order to develop some intuition about the information encompassed in Eq. (13), we study its behavior in a few simple distributions of matter, velocity, and magnetic field. It should be noted that the indexes i and j represent the axes of a 3D Cartesian reference frame, thus $i = 0, 1,$ and 2 correspond to the x -, y -, and z -axis, respectively.

3.1.1. Strong magnetic field

If we consider a very strong magnetic field with respect to the turbulent motions, such that \mathbf{B} is oriented almost exclusively along the x -axis, and a converging flow¹ along the same direction, Eq. (13) reduces to

$$\frac{d(\cos \phi)}{dt} \simeq \partial_0 v_0 (r_0 r_0 - 1) \cos \phi, \quad (18)$$

where we ignore the terms depending on $\partial_i(\partial_j v_j)$, which are on average much smaller than those related to $\partial_i v_j$, as will be shown in Sect. 3.2. Given that $r_0^2 < 1$, $\partial_0 v_0 (r_0 r_0 - 1) > 0$ and $\cos \phi \rightarrow \pm 1$. That is to say, the contraction along the field lines tends to align the density gradient and the magnetic field.

If we consider the same configuration of \mathbf{B} , but this time consider a convergent flow perpendicular to its mean direction, Eq. (13) reduces to

$$\frac{d(\cos \phi)}{dt} \simeq \partial_1 v_1 (r_1 r_1) \cos \phi. \quad (19)$$

In this case, $\cos \phi \rightarrow 0$ since the term in front of the cosine is negative.

3.1.2. Weak magnetic field

We consider now a magnetic field that is weak with respect to the turbulent motions, a matter initially distributed in a slab perpendicular to the x -axis, and a converging flow along the same direction. Assuming again that the second-order spatial derivatives are negligible, Eq. (13) reduces to

$$\frac{d(\cos \phi)}{dt} \simeq \partial_i v_j (r_i r_j - b_i b_j) \cos \phi. \quad (20)$$

Equation (20) implies that in the case of single compressive flow, the change in relative orientation is the result of two competing terms. The first, $r_i r_j$, which in this particular configuration is non-zero only for $i = 0$, indicates the geometrical distribution of ρ and the second, $b_i b_j$, indicates the distribution of the magnetic field orientation and tends to be larger when the field is stronger. Given that here $\partial_0 v_0 < 0$, which is implied from the converging flow assumption, and in the case of a weak field $b_i b_i$ is on average equal to $1/3$, Eq. (20) leads to

$$\frac{d(\cos \phi)}{dt} \propto -\cos \phi, \quad (21)$$

which has solutions that tend towards $\cos \phi = 0$.

Alternatively, if we consider the same ρ and \mathbf{B} configurations as in the previous example, but this time a converging flow along the y -axis, Eq. (13) reduces to

$$\frac{d(\cos \phi)}{dt} \simeq -\partial_1 v_1 b_1 b_1 \cos \phi. \quad (22)$$

¹ In the general case, a converging flow is defined by $\det(\partial_i v_i) < 0$.

This expression shows that, in this particular example, the relative orientation between $\nabla\rho$ and \mathbf{B} changes by effect of the y -axis component of the magnetic field. Thus, it implies that even if the magnetic field is weak, motions strictly along the field lines tend to create density structures perpendicular to it.

3.1.3. Analytical hints on the relative orientation

Since the strain tensor $(\partial_i v_j + \partial_j v_i)/2$ is symmetric, there are at least three mutually perpendicular directions with respect to which the matrix of $(\partial_i v_j + \partial_j v_i)/2$ is diagonal. Geometrically, this means that infinitesimal line elements in these directions remain mutually perpendicular after deformation. These directions are known as principal directions (Lai et al. 2010). If we consider the basis where the strain tensor is diagonal, the principal-directions basis, Eq. (17) can be expressed as

$$A_{23} = \lambda_i(r_i^2 - b_i^2), \quad (23)$$

where λ_i are the eigenvalues of the strain tensor.

For the sake of illustration, we can reduce the problem to 2D and consider two eigenvalues, one negative (λ_c), which is dominant if we consider the case where $\partial_i v_i < 0$, and one positive (λ_s). In general terms, the fluid parcel is compressed in the direction associated with λ_c and stretched in the other. It can therefore be represented as an ellipsoid whose short axis corresponds to the direction associated with λ_c and whose major axis to the direction associated with λ_s . Given that r_i is a gradient, it is larger along the short axis, that is, the direction associated with λ_c .

If the magnetic field is weak, \mathbf{B} tends to be parallel to the major axis of the ellipsoid, because the field is compressed by the converging flow. That means that b_c is small and A_{23} is negative, thus taking the system towards the $\cos\phi = 0$ configuration. If the field is strong, the compression occurs mainly along the field lines, thus making \mathbf{B} parallel to the short axis of the ellipsoid. In this case, $A_{23} \simeq \lambda_c(r_c^2 - b_c^2)$, so the sign depends on the respective values of r_c^2 and b_c^2 . In the limit where \mathbf{B} is very strong, one expects the field lines to be straight and \mathbf{B} more organized than $\nabla\rho$, thus $r_c^2 - b_c^2 < 0$.

These simple cases correspond to highly idealized flows and magnetic field configurations. To study configurations where the magnetic field is not infinitely rigid or the flow has more than one single compressive component, we need to consider a realization of a turbulent flow in a molecular cloud, which is accessible through the numerical simulation of MHD turbulence.

3.2. Simulation of magnetohydrodynamic turbulence

We consider the simulations of MHD turbulence introduced in Dib et al. (2010) and used in Soler et al. (2013). These simulations correspond to a 4-parsec-side periodic box with mean number density $n = 536 \text{ cm}^{-3}$, and include the effect of self-gravity, magnetic field, and decaying turbulence. The medium inside the box is isothermal ($T = 11.4 \text{ K}$) and has an initial sonic Mach number $\mathcal{M}_s = 10$. These simulations were computed in an adaptive mesh refinement (AMR) grid with maximum resolution of 2^{-9} pc and we analyze them in a regular grid with 2^{-7} pc resolution. For the sake of simplicity, we consider only two snapshots taken at 1/3 and 2/3 of the flow crossing time.

This set of simulations includes realizations with three initial degrees of magnetization, quantified in terms of the ratio of the thermal to magnetic pressure, β ; quasi-hydrodynamic, $\beta_0 = 100$; equipartition, $\beta_0 = 1.0$; and strong magnetic field, $\beta_0 = 0.1$. Soler et al. (2013) reported that in 3D, the change in the relative

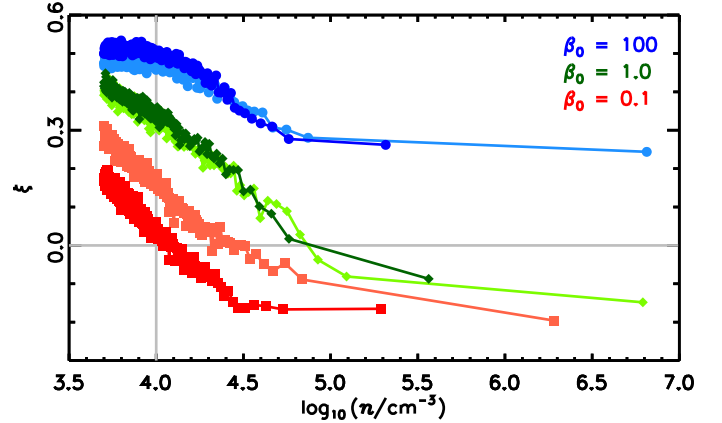


Fig. 1. Relative orientation parameter, ξ , as a function of particle density, $n \equiv \rho/\mu$, in the simulations used in Soler et al. (2013). The values of ξ correspond to the relative orientation between $\nabla\rho$ and \mathbf{B} in n -bins with an equal number of voxels, all with $n > 500 \text{ cm}^{-3}$. The values $\xi > 0$ correspond to $\nabla\rho$ mostly perpendicular to \mathbf{B} and $\xi < 0$ correspond to $\nabla\rho$ mostly parallel to \mathbf{B} . The gray horizontal line is $\xi = 0$, which corresponds to the case where there is no preferred relative orientation between $\nabla\rho$ and \mathbf{B} . The darker colors represent the early snapshots in the simulation and the lighter colors represent the later snapshots. The gray vertical line, drawn for reference, corresponds to $n = 10^4 \text{ cm}^{-3}$.

orientation between the magnetic field \mathbf{B} and the iso-density contours, inferred from $\nabla\rho$, is related to the initial degree of magnetization. In the realizations with $\beta_0 = 0.1$ and $\beta_0 = 1.0$, which correspond to sub-Alfvénic or close to equipartition turbulence, $\cos\phi$ changes from being mostly zero at low densities to being mostly plus or minus one at the highest densities. In the realization with $\beta_0 = 100$, super-Alfvénic turbulence, $\cos\phi$ is mostly zero at all densities. Both of these results were expressed in terms of the relative orientation parameter (ξ), which corresponds to the difference between the number of voxels where $\cos\phi \approx 0$ minus the number of voxels where $\cos\phi \approx \pm 1$ divided by the total number of voxels where $\cos\phi \approx 0$ or $\cos\phi \approx \pm 1$, as explicitly described in equation 4 of Planck Collaboration Int. XXXV (2016). Consequently, ξ is positive if $\cos\phi$ is mostly equal to zero, i.e., $\nabla\rho$ mostly perpendicular to \mathbf{B} , and negative if $|\cos\phi|$ is mostly one, i.e., $\nabla\rho$ mostly parallel to \mathbf{B} .

In order to illustrate the interpretation of Eq. (13), we reproduce the relative orientation between \mathbf{B} and the iso- ρ contours presented in Soler et al. (2013) for the range of densities $n > 5 \times 10^2 \text{ cm}^{-3}$. We estimated $\nabla\rho$ using a Lagrange 5-points interpolation to express each ρ data point in the simulation cube as a point on a polynomial and then differentiate that polynomial². The mean values of ξ in different density bins, presented in Fig. 1, illustrate the different trends in relative orientation between $\nabla\rho$ and \mathbf{B} for different initial magnetizations. Given that $n \equiv \rho/\mu$ and μ , the mean particle mass, is constant in the simulations, we choose to report these results in terms of n without any loss of generality.

Figure 2 shows that in the same density range, the negative values of ξ are associated with $\nabla \cdot \mathbf{v} < 0$ in the simulations with $\beta_0 = 0.1$ and $\beta_0 = 1.0$. However, this is not the case for the $\beta_0 = 100$ simulations, thus showing that $\nabla \cdot \mathbf{v} < 0$ is not the only condition producing the change in the relative orientation between $\nabla\rho$ parallel to \mathbf{B} . Furthermore, Fig. 2 illustrates that in the simulations with $\beta_0 = 0.1$ and $\beta_0 = 1.0$, the transition

² pdiv.pro routine developed by Chris Beaumont (<https://github.com/ChrisBeaumont>).

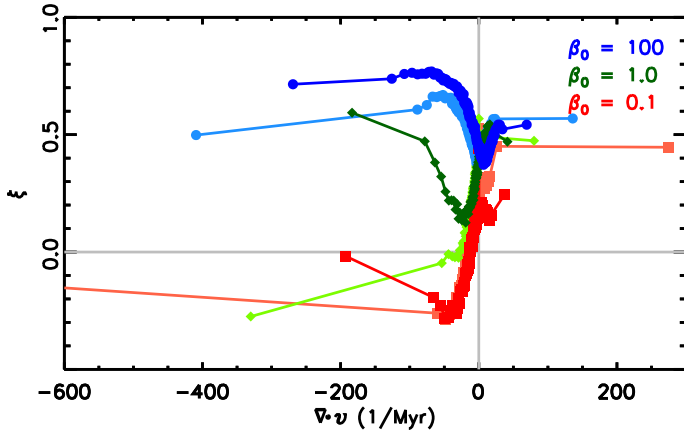


Fig. 2. Relative orientation parameter, ξ , as a function of the velocity divergence, $\nabla \cdot \mathbf{v} \equiv \partial_i v_i$, in the simulations introduced in Soler et al. (2013). The values of ξ correspond to the relative orientation between $\nabla \rho$ and \mathbf{B} in $\nabla \cdot \mathbf{v}$ -bins with an equal number of voxels, all with $n > 500 \text{ cm}^{-3}$. The colors and the symbols follow the conventions introduced in Fig. 1. The gray vertical line, drawn for reference, corresponds to $\nabla \cdot \mathbf{v} = 0 \text{ Myr}^{-1}$.

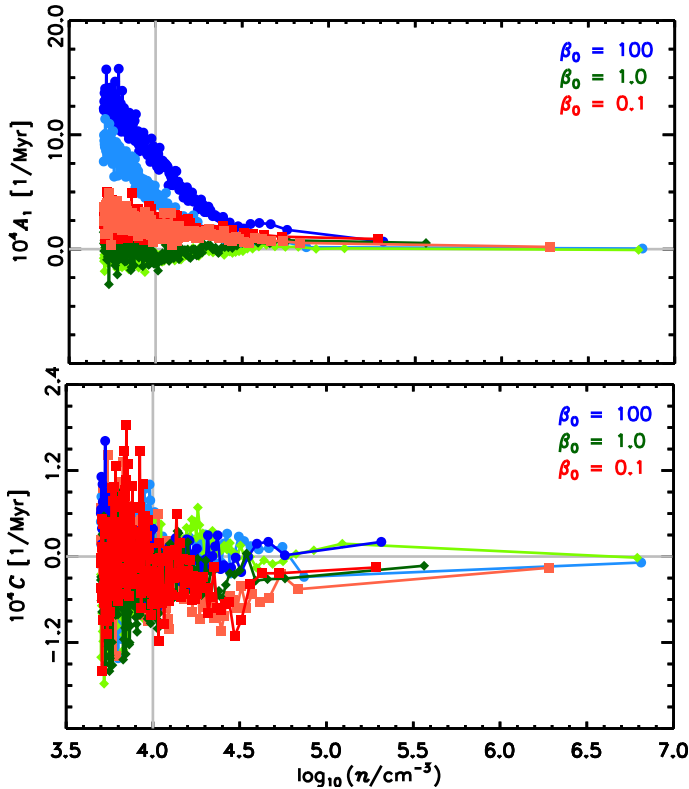


Fig. 3. Mean values of $10^4 A_1$ (top) and $10^4 C$ (bottom) as a function of particle density, n , in the simulations introduced in Soler et al. (2013). The values of A_1 and C correspond to the definitions in Eqs. (14) and (15), respectively. The gray vertical line, drawn for reference, corresponds to $n = 10^4 \text{ cm}^{-3}$.

between $\xi > 0$ or $\cos \phi = 0$, and $\xi < 0$ or $\cos \phi = \pm 1$, happens across $\nabla \cdot \mathbf{v} = 0$, but ξ is not strictly negative until the second snapshot, when the values of $\nabla \cdot \mathbf{v}$ are more negative.

We further quantify the source of change in relative orientation in the simulations with $\beta_0 = 1$ and $\beta_0 = 0.1$ by focusing on the behavior of the coefficients C , A_1 , and A_{23} in Eq. (13). Figures 3 and 4 show the values of C , A_1 , and A_{23} in bins of n

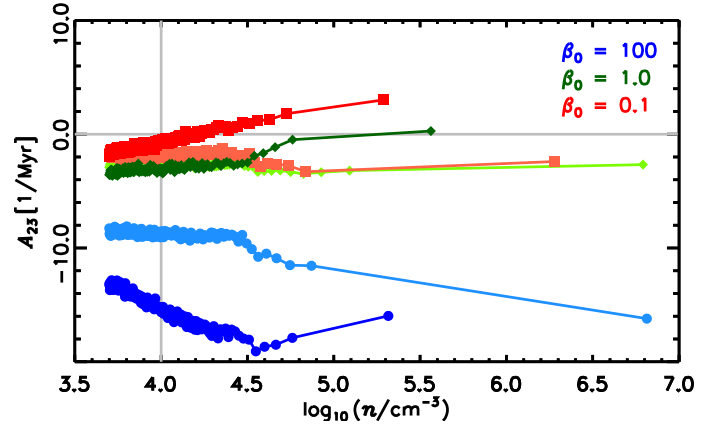


Fig. 4. Mean values of the term A_{23} , defined in Eq. (23), as a function of particle density, n , in the simulations introduced in Soler et al. (2013). The gray vertical line, drawn for reference, corresponds to $n = 10^4 \text{ cm}^{-3}$.

with an equal number of voxels. The values shown in the figures confirm that C and A_1 are considerably smaller than the values of A_{23} , which is expected given that the former depends on second-order spatial derivatives of the velocity field, while the latter depend on first-order derivatives. Additionally, the values of both C and A_1 fluctuate around zero, thus making their mean values small with respect to A_{23} .

Given that $A_{23}/C \approx A_{23}/A_1 \approx 10^4$, Eq. (13) reduces to

$$\frac{d(\cos \phi)}{dt} \approx A_{23} \cos \phi, \quad (24)$$

which implies that the change in relative orientation depends mainly on the sign of A_{23} . If $A_{23} < 0$, $\cos \phi$ tends to decrease towards 0, which corresponds to \mathbf{B} being perpendicular to $\nabla \rho$. If $A_{23} > 0$, $\cos \phi$ tends to increase towards ± 1 , which corresponds to \mathbf{B} being parallel to $\nabla \rho$.

A comparison between Figs. 1 and 4 indicates that the change in relative orientation between $\nabla \rho$ and \mathbf{B} in the first snapshot of the simulations for $\beta_0 = 1$ and the $\beta_0 = 0.1$ happens around the same n values where A_{23} changes its sign. In contrast, in the $\beta_0 = 100$ simulation, where there is no change in relative orientation, the values of A_{23} are always negative. In the second snapshot, Fig. 4 reveals that A_{23} is negative for the equipartition and high-magnetization simulations and accordingly, the perpendicular relative orientation at the highest densities is less prominent than in the first snapshot.

Given the transformation to the principal-directions basis, \mathcal{D} , we write Eq. (17) as

$$A_{23} = \frac{1}{2} \mathcal{D}[\partial_i(v_j) + \partial_j(v_i)] \mathcal{D}^{-1} \mathcal{D}[r_i r_j - b_i b_j] \mathcal{D}^{-1}, \quad (25)$$

which reduces to

$$A_{23} = \lambda_i \delta_{ij} \mathcal{D}[r_i r_j - b_i b_j] \mathcal{D}^{-1}, \quad (26)$$

where λ_i are the three eigenvalues of $(\partial_i v_j + \partial_j v_i)/2$ and δ_{ij} is the Kronecker delta.

The eigenvalues (λ_i) correspond to the unit strain along each of the principal directions. Thus, the eigenvector associated with the highest eigenvalue describes the axis along which the infinitesimal fluid parcel is mostly elongated. The two other eigenvectors, which are associated with the two other eigenvalues,

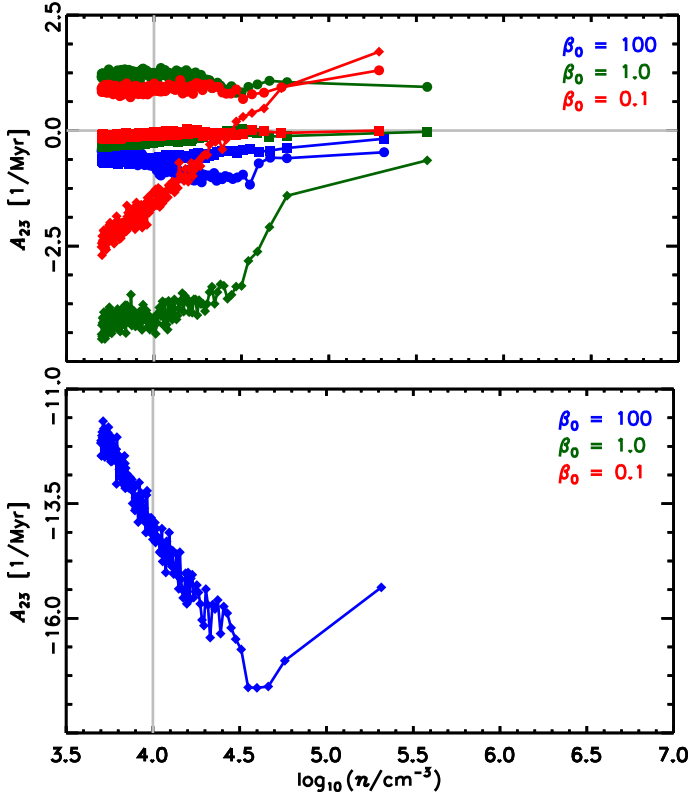


Fig. 5. Mean values of the principal components of A_{23} , defined in Eq. (26), as a function of density, n , in the simulations introduced in Soler et al. (2013). The component associated with the most negative eigenvalue of the symmetric part of the strain tensor, which corresponds to the dominant compressive mode, is represented by the diamonds. These values are outside of the range in the case of the $\beta_0 = 100$ simulation, thus they are presented separately in the lower panel. The intermediate and maximum eigenvalues are represented by circles and squares, respectively.

correspond to the directions along which the shape of the infinitesimal fluid parcel is either stretched or compressed, depending on their signs (Lai et al. 2010).

We diagonalize the strain tensor in each position of the simulation cube and computed the A_{23} terms associated with each of its eigenvalues, as described in Eq. (26). The mean value of each of these terms in density bins with an equal number of voxels is presented in Fig. 5. In the low-magnetization simulation, all three components of A_{23} are negative and although one of them is clearly different, which can be associated to some degree with the anisotropy produced by the magnetic field, their sign implies that all of them contribute to keep the $\cos \phi = 0$ configuration. In the equipartition and high-magnetization simulations, the component of A_{23} associated with the most negative eigenvalue, which traces the main compressive mode, increases its mean value with increasing density. This can be interpreted in similar terms to those described in Sect. 3.1.3: $\partial_i v_i$ is mostly negative, so A_{23} remains negative as long as the correlation between the orientation of the magnetic field components, represented by $b_i b_j$ is smaller than that of the density gradient represented by $r_i r_j$. Once $b_i b_j$ becomes larger than $r_i r_j$ by the effect of the compression of the magnetized medium, the sign of A_{23} changes and the system changes towards the $\cos \phi = \pm 1$ configuration.

4. Discussion

4.1. What changes when the relative orientation between $\nabla \rho$ and \mathbf{B} changes?

The clear anisotropy produced by the magnetic field in the velocity and the density distributions is expected, at least in the case of incompressible turbulence (Goldreich & Sridhar 1995). However, the reasons why compressible MHD turbulence produces structures in particular configurations with respect to the magnetic field were less clear.

Hennebelle (2013) shows that non-self-gravitating filaments are a generic consequence of turbulent strains in a magnetized medium and their elongation along the magnetic field lines by effect of the Lorentz force helps to keep them coherent. The fact that the shear modes are mostly responsible for the observed and simulated stretching of matter along the magnetic field, is confirmed by the $\cos \phi = 0$ equilibrium point of Eq. (13), which is the dominant in the case that $\partial_i v_i$ is small. The $\cos \phi = \pm 1$ equilibrium point of Eq. (13), explains why the change in relative orientation is observed at the highest densities: it is produced by the compressive modes that produce the accumulations of matter. In the light of Eq. (13), the question is not what produces the relative orientation but rather what makes it change and how we can use that information to learn about the magnetic field in MCs.

Chen et al. (2016) describes the transition density, from $\cos \phi = 0$ to $\cos \phi = \pm 1$, as a threshold for the gravity-driven Alfvénic transition from sub- to super-Alfvénic turbulence. This transition in relative orientation is indeed expected; if the turbulence is sub-Alfvénic, slow modes are important and they tend to be anti-correlated with the density field, while it is the contrary for super-Alfvénic turbulence, where fast modes are dominant. This interpretation is not easy to generalize to the ISM, where dense structures are the result of multiple shocks induced by the super-Alfvénic turbulence and the structure of the magnetic field may be inherited from the very large scales. Moreover, it is not clear to what extent one can unambiguously separate regions into sub- and super-Alfvénic turbulence.

For the sake of the discussion, we estimated the relative orientation parameter in bins of Alfvén Mach number, $\mathcal{M}_A \equiv \sigma_v/v_A = \mathcal{M}_S \beta^2$, in the considered set of simulations. If the transition from $\cos \phi = 0$ to $\cos \phi = \pm 1$ were related to the transition from sub-Alfvénic to super-Alfvénic turbulence, one should expect that the regions where $\mathcal{M}_A < 1$ would be associated with $\xi > 0$ and the regions where $\mathcal{M}_A > 1$ would be associated with $\xi < 0$. Figure 6 shows that this is not necessarily the case in the considered simulations. In the realization with $\beta_0 = 100$, there is a transition from $\mathcal{M}_A < 1$ to $\mathcal{M}_A > 1$, due to the increase in velocity dispersions as a product of the gravitational collapse into denser structures, but there is no change in the sign of ξ . The realization with $\beta_0 = 0.1$, show that the $\xi < 0$ values are indeed associated with regions where $\mathcal{M}_A > 1$, but that $\mathcal{M}_A > 1$ does not necessarily imply $\xi > 0$, thus indicating that there must be another quantity that is more directly responsible for the change in relative orientation between $\nabla \rho$ and \mathbf{B} .

Equation (13) and the results of the analysis presented in Sect. 3.2 suggest that the change between $\cos \phi = 0$ and $\cos \phi = \pm 1$, or from $\nabla \rho$ being predominantly perpendicular to being predominantly parallel to \mathbf{B} , are related to the tensors composing the coefficient A_{23} , as stated by Eq. (17). If $A_{23} < 0$, the flow tends towards the $\cos \phi = 0$ configuration; the change in that tendency in the case of a predominantly converging flow, $\partial_i v_i < 0$, is related to the change of sign in the tensor $(r_i r_j - b_i b_j)$. Thus, we can infer that the density threshold where $\cos \phi$ changes is linked to

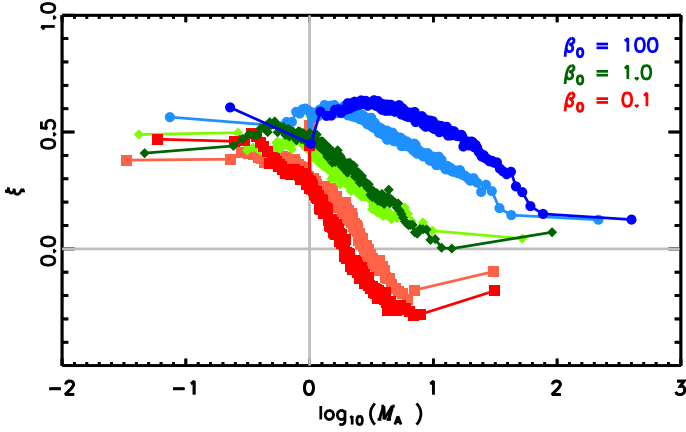


Fig. 6. Relative orientation parameter, ξ , as a function of the Alfvén Mach number, M_A , in the simulations introduced in Soler et al. (2013). The darker colors represent the early snapshots in the simulation and the lighter colors represent the later snapshots. The values $\xi > 0$ correspond to $\nabla\rho$ mostly perpendicular to \mathbf{B} and $\xi < 0$ correspond to $\nabla\rho$ mostly parallel to \mathbf{B} . The gray horizontal line is $\xi = 0$, which corresponds to the case where there is no preferred relative orientation between $\nabla\rho$ and \mathbf{B} . The gray vertical line, drawn for reference, corresponds to $M_A = 1$, which marks the border between sub-, $M_A < 1$, and super-Alfvénic, $M_A > 1$, turbulence.

the relation between the $r_i r_j$ and the $b_i b_j$ tensors, which is clearly dependent on the initial magnetization.

Figure 7 presents the distributions of ρ and the \mathbf{B} orientation, A_{23} , and M_A in a slice of the first snapshot of the simulations with weak, $\beta_0 = 100$, and strong $\beta_0 = 0.1$ initial magnetization. The upper panel illustrates how \mathbf{B} clearly follows the density structure in the simulation with $\beta_0 = 100$ and how \mathbf{B} is more homogeneous in the simulations where $\beta_0 = 0.1$. For the sake of completeness, we also present the values of M_A in the middle panel of Fig. 7. The figure shows that the values of M_A in the lower density regions of the slice correspond to the initial magnetizations, that is, $M_A > 1$ in the $\beta_0 = 100$ and $M_A < 1$ in the $\beta_0 = 0.1$ case. At higher densities, however, these values change and some density structures in the $\beta_0 = 100$ case present $M_A \approx 1$ and some density structures in the $\beta_0 = 0.1$ case show $M_A \gtrsim 1$. Both cases, illustrate that the change in relative orientation is not straightforward in some particular structures in the map, but it is rather a statistical trend that is better summarized in the analysis presented in Fig. 6.

Finally, the bottom panel of Fig. 7 shows the distribution of A_{23} , the terms whose sign determines the changes in the relative orientation between $\nabla\rho$ and \mathbf{B} . In the case with low initial magnetization, A_{23} is clearly organized in filaments that correspond to many of those seen in the density map. The presence of regions where $A_{23} > 0$ indicates that there are zones where the relative orientation between $\nabla\rho$ and \mathbf{B} tends to change, although the average values in particular density ranges shows a general tendency towards the $\cos\phi = 0$ configuration. In the case with high initial magnetization, A_{23} is more inhomogeneous and the density structures do not have clear counterparts in A_{23} . The presence of extended regions with both positive and negative values of A_{23} shows that the change in relative orientation is a dynamic process that is not localized in a few structures but rather a statistical trend that becomes evident when analyzing particular density ranges, as shown in Fig. 5.

4.2. Relative orientation and scaling of the magnetic field with increasing density

Observations of the Zeeman effect indicate that in the diffuse lines of sight ($N_H \lesssim 10^{21.5} \text{ cm}^{-2}$), the maximum magnetic field strength B_{max} sampled by HI lines does not scale with density. In the denser regions ($N_H \gtrsim 10^{21.5} \text{ cm}^{-2}$) probed by OH and CN spectral lines the same study reports a scaling of the maximum magnetic field strength $B_{\text{max}} \propto n^{0.65}$ (Crutcher et al. 2010; Crutcher 2012, and references therein). The former observation can be interpreted as the effect of diffuse clouds assembled by flows along magnetic field lines, which would increase the density but not the magnetic field strength. The latter observation can be interpreted as the effect of isotropic contraction of weakly magnetized gas. Probably related to these interpretations is the fact that the column density where the magnetic field strength starts scaling with increasing column density is very close to the column densities where Planck Collaboration Int. XXXV (2016) identified the change in relative orientation from $\langle \hat{\mathbf{B}}_{\perp} \rangle$ mostly parallel to the iso- N_H contours to mostly perpendicular.

The column density values around which the Zeeman observations show the scaling of the magnetic field with increasing density are indeed very close to the column densities where the relative orientation between the column density structures and the magnetic field, inferred from the dust polarization observations, changes from mostly parallel to mostly perpendicular. This similarity has been identified in the colliding flow models presented in Chen et al. (2016), where it is assigned to the beginning of gravity-induced acceleration in terms of increasing gas velocity with density. As discussed here, this may not necessarily be the case.

5. Conclusions

We studied the relative orientation between $\nabla\rho$ and \mathbf{B} using the transport equations of MHD turbulence. Under the assumptions of flux freezing and low magnetic diffusivity, we arrived at Eq. (13), which is an expression that describes the evolution of $\cos\phi$, the cosine of the angle between $\nabla\rho$ and \mathbf{B} .

From the study of Eq. (13) we conclude the following:

1. The configuration where $\cos\phi = \pm 1$ is a generic equilibrium point, a configuration towards which the system tends to evolve and a potential attractor.
2. The configuration where the $\cos\phi = 0$ constitutes another equilibrium point.
3. The changes in the relative orientation are produced by the coupling of the strain tensor $\partial_i v_j$ and the $r_i r_j$ and $b_i b_j$ tensors, defined in Eqs. (7) and (8), which correspond to the autocorrelations of the density gradient and magnetic field orientations, respectively.

Using the simulations of MHD turbulence used in Soler et al. (2013), we show the following:

1. The configuration $\cos\phi = 0$ is dominant at all densities in the quasi-hydrodynamic simulation ($\beta_0 = 100$) and in all but the highest densities in the initially equipartition ($\beta_0 = 1.0$) and high-magnetization ($\beta_0 = 0.1$) simulations, as illustrated in Fig. 1.
2. The $\cos\phi = \pm 1$ is only present in the regions where $\partial_i v_i < 0$ in the $\beta_0 = 1.0$ and $\beta_0 = 0.1$ simulations, as shown in Fig. 2.
3. The density over which $\cos\phi$ changes from 0 to ± 1 in the $\beta_0 = 1.0$ and $\beta_0 = 0.1$ simulations corresponds to that where the term A_{23} changes its sign, as illustrated in Fig. 4

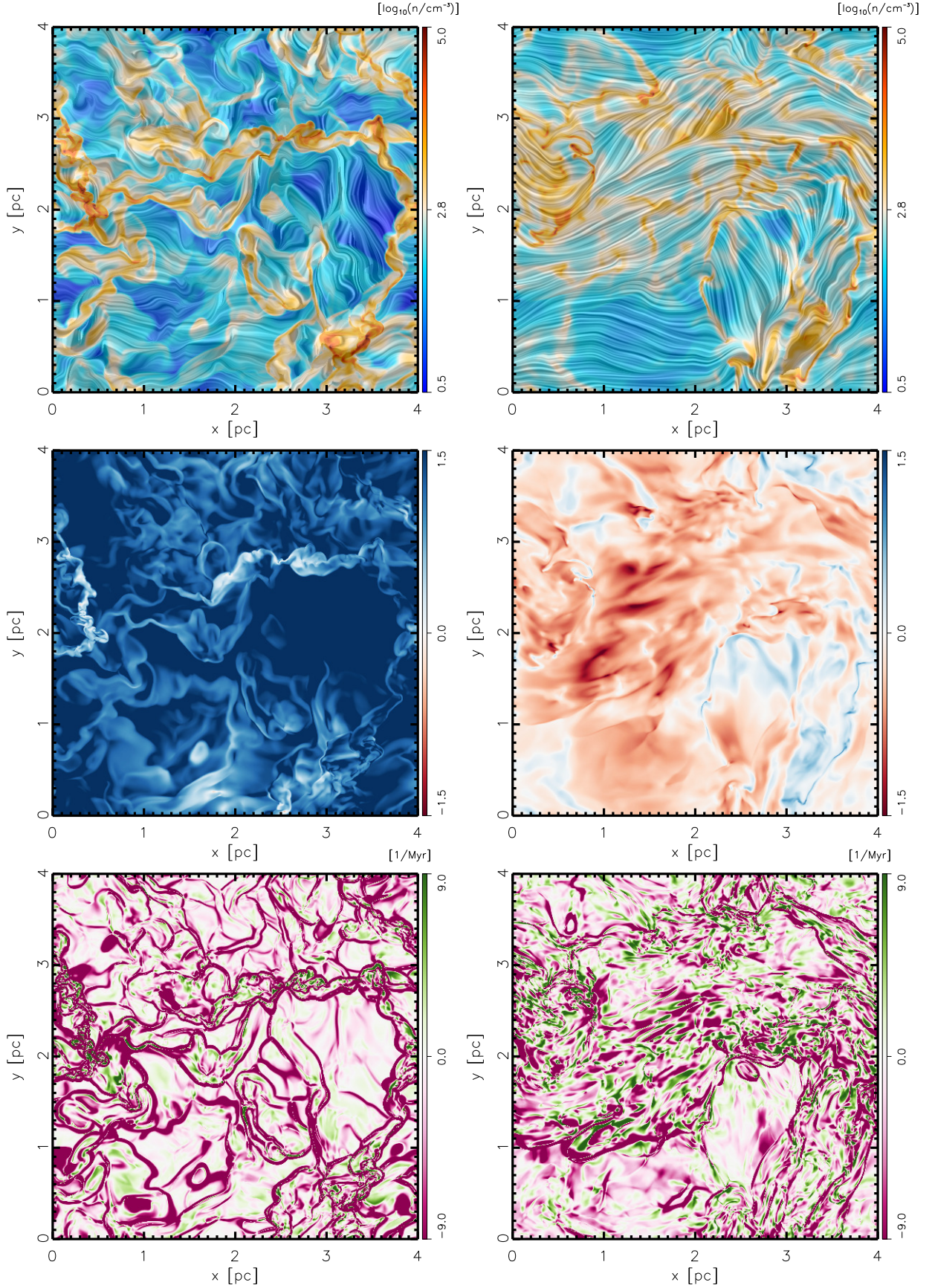


Fig. 7. Distributions of the density and magnetic field (*top*), the logarithm of the Alfvén Mach number M_A (*middle*), and the coefficient A_{23} of Eq. (13) (*bottom*) in a slice ($z = 256$) of the MHD turbulence simulations used in Soler et al. (2013) for initially weak ($\beta = 100$, *left*) and strong ($\beta = 0.1$, *right*) magnetic field in a snapshot taken at one-third of the flow crossing time. The coefficient A_{23} is the term dominating the change in the relative orientation between $\nabla\rho$ and \mathbf{B} according to Eq. (13).

4. In the case of $\det(\partial_i v_j) < 0$, which corresponds to a converging flow, the change of sign in A_{23} occurs when the $b_i b_j$ tensor dominates over $r_i r_j$.
5. The density over which A_{23} changes sign, bringing the system from the $\cos \phi = 0$ to the $\cos \phi = \pm 1$, depends on the strength of the initial magnetic field.
6. The changes in $\cos \phi$ are mainly related to the compressive modes of the strain tensor $\partial_i v_j$ and their coupling to a relatively strong magnetic field with respect to the turbulent motions, as illustrated in Fig. 5, and not to a clear transition in the Alfvén Mach number, as shown in Fig. 6.

These results indicate that, once the projection effects are properly accounted for, the observations of the relative orientation between column density structures and the projected magnetic field can be interpreted as follows:

1. The observed low-density structures aligned with the magnetic field are spontaneously produced in regions where shear motions are dominant over compression.
2. The observed change in relative orientation between the N_H structures and $\langle \hat{\mathbf{B}}_{\perp} \rangle$ towards molecular clouds is an indication of compressive motions, that is, $\partial_i v_i < 0$, which can be the result of either gravitational collapse or converging flows.
3. The density threshold at which the relative orientation between the N_H structures and $\langle \hat{\mathbf{B}}_{\perp} \rangle$ changes from mostly parallel to mostly perpendicular depends on the field strength and not necessarily on the strength of the compressive motions.

We have shown that the relative orientation between density structures and the magnetic field are related to the dynamics of MHD turbulence, particularly to the contraction motions and the degree of magnetization. Although the astronomical data are two-dimensional in nature and incorporate signal integrations along the line of sight and across the telescope beam, our calculations suggest that there is a theoretical basis for interpreting the observed changes in the relative orientation between N_H structures and $\langle \hat{\mathbf{B}}_{\perp} \rangle$ towards molecular clouds as the imprint of the magnetic field playing a significant role in the assembly of the parcels of gas that produce molecular clouds. While a direct estimate of the magnetic field strength using the relative orientation between N_H structures and $\langle \hat{\mathbf{B}}_{\perp} \rangle$ remains elusive, it is clear that the study of this and other statistical correlations is crucial for constraining the range of scales and densities where the magnetic field is shaping the structure of the ISM.

Acknowledgements. This work was made possible through the funding from the European Research Council under the European Community's Seventh Framework Programme (FP7/2007-2013 Grant Agreement Nos. 306483 and 291294). J.D.S. acknowledges support from the European Research Council under the Horizon 2020 Framework Program via the ERC Consolidator Grant

CSF-648505. We thank the referee Martin Houde for his insightful comments that helped to improve this work. Additionally, we thank the following people who helped with their encouragement and conversation: Henrik Beuther, François Boulanger, Jouni Kainulainen, Ralf Klessen, and Alex Lazarian.

References

- Banerjee, R., Vázquez-Semadeni, E., Hennebelle, P., & Klessen, R. S. 2009, *MNRAS*, **398**, 1082
- Bergin, E. A., & Tafalla, M. 2007, *ARA&A*, **45**, 339
- Boldyrev, S. 2006, *Phys. Rev. Lett.*, **96**, 115002
- Chen, C.-Y., King, P. K., & Li, Z.-Y. 2016, *ApJ*, **829**, 84
- Clark, S. E., Peek, J. E. G., & Putman, M. E. 2014, *ApJ*, **789**, 82
- Crutcher, R. M. 2012, *ARA&A*, **50**, 29
- Crutcher, R. M., Wandelt, B., Heiles, C., Falgarone, E., & Troland, T. H. 2010, *ApJ*, **725**, 466
- Dib, S., Hennebelle, P., Pineda, J. E., et al. 2010, *ApJ*, **723**, 425
- Field, G. B. 1965, *ApJ*, **142**, 531
- Goldreich, P., & Sridhar, S. 1995, *ApJ*, **438**, 763
- González-Casanova, D. F., & Lazarian, A. 2017, *ApJ*, **835**, 41
- Hartmann, L., Ballesteros-Paredes, J., & Bergin, E. A. 2001, *ApJ*, **562**, 852
- Heiles, C., & Crutcher, R. 2005, in *Cosmic Magnetic Fields*, eds. R. Wielebinski, & R. Beck (Berlin: Springer Verlag), Lect. Notes Phys., 664, 137
- Hennebelle, P. 2013, *A&A*, **556**, A153
- Hennebelle, P., & Falgarone, E. 2012, *A&ARv*, **20**, 55
- Hennebelle, P., & Pérault, M. 2000, *A&A*, **359**, 1124
- Heyer, M., Gong, H., Ostriker, E., & Brunt, C. 2008, *ApJ*, **680**, 420
- Heyer, M., Goldsmith, P. F., Yıldız, U. A., et al. 2016, *MNRAS*, **461**, 3918
- Hoq, S., Clemens, D. P., Guzmán, A. E., & Cashman, L. R. 2017, *ApJ*, **836**, 199
- Houde, M., Vaillancourt, J. E., Hildebrand, R. H., Chitsazzadeh, S., & Kirby, L. 2009, *ApJ*, **706**, 1504
- Iffrig, O., & Hennebelle, P. 2017, *A&A*, **604**, A70
- Inoue, T., Inutsuka, S.-I., & Koyama, H. 2007, *ApJ*, **658**, L99
- Kalberla, P. M. W., Kerp, J., Haud, U., et al. 2016, *ApJ*, **821**, 117
- Klessen, R. S., & Glover, S. C. O. 2016, *Star Formation in Galaxy Evolution: Connecting Numerical Models to Reality*, Saas-Fee Advanced Course (Berlin Heidelberg: Springer-Verlag), 43, 85
- Körtgen, B., & Banerjee, R. 2015, *MNRAS*, **451**, 3340
- Kusune, T., Sugitani, K., Nakamura, F., et al. 2016, *ApJ*, **830**, L23
- Lai, W. M., Rubin, D., & Krempf, E. 2010, *Introduction to Continuum Mechanics*, 4th edn. (Butterworth-Heinemann)
- Landau, L. D., Pitaevskii, L. P., Kosevich, A. M., & Lifshitz, E. M. 1986, *Theory of Elasticity (Course of Theoretical Physics)*, 3rd edn. (Butterworth-Heinemann), 7
- Li, H.-B., Fang, M., Henning, T., & Kainulainen, J. 2013, *MNRAS*, **436**, 3707
- Malinen, J., Montier, L., Montillaud, J., et al. 2016, *MNRAS*, **460**, 1934
- Mathaeus, W. H., Pouquet, A., Mininni, P. D., Dmitruk, P., & Breech, B. 2008, *Phys. Rev. Lett.*, **100**, 085003
- Palmeirim, P., André, P., Kirk, J., et al. 2013, *A&A*, **550**, A38
- Passot, T., Vázquez-Semadeni, E., & Pouquet, A. 1995, *ApJ*, **455**, 536
- Planck Collaboration I. 2016, *A&A*, **594**, A1
- Planck Collaboration Int. XXXII. 2016, *A&A*, **586**, A135
- Planck Collaboration Int. XXXV. 2016, *A&A*, **586**, A138
- Santos, F. P., Busquet, G., Franco, G. A. P., Girart, J. M., & Zhang, Q. 2016, *ApJ*, **832**, 186
- Soler, J. D., Hennebelle, P., Martin, P. G., et al. 2013, *ApJ*, **774**, 128
- Soler, J. D., Alves, F., Boulanger, F., et al. 2016, *A&A*, **596**, A93
- Soler, J. D., Ade, P. A. R., Angilè, F. E., et al. 2017, *A&A*, **603**, A64
- Sugitani, K., Nakamura, F., Watanabe, M., et al. 2011, *ApJ*, **734**, 63
- Yuen, K. H., & Lazarian, A. 2017, *ApJ*, **837**, L24

Appendix A: Relative orientation between \mathbf{B} and \mathbf{v}

Following a similar procedure to that described in Sect. 2.1, we obtained an expression for the relative orientation between the magnetic field, \mathbf{B} , and the velocity, \mathbf{v} ,

$$\cos \theta = \frac{v_i B_i}{(v_k v_k)^{1/2} (B_i B_i)^{1/2}}. \quad (\text{A.1})$$

Using the definitions,

$$u_i \equiv \frac{v_i}{(v_k v_k)^{1/2}} \quad (\text{A.2})$$

and

$$b_i \equiv \frac{B_i}{(B_k B_k)^{1/2}}, \quad (\text{A.3})$$

we obtain

$$\begin{aligned} \frac{d \cos \theta}{dt} &= u_i \frac{db_i}{dt} + b_i \frac{du_i}{dt} \\ &= \frac{(u_i - b_i \cos \theta) dB_i}{(B_k B_k)^{1/2}} + \frac{(b_i - u_i \cos \theta) dv_i}{(v_k v_k)^{1/2}}. \end{aligned} \quad (\text{A.4})$$

We consider the Cauchy momentum equation in a magnetized fluid to obtain

$$\frac{dv_i}{dt} = -\frac{1}{\rho} \left[\partial_i P + B_j \partial_j B_i - B_j \partial_i B_j \right]. \quad (\text{A.5})$$

Combining the continuity and the Faraday equation results in

$$\frac{d(B_i/\rho)}{dt} = \frac{B_j}{\rho} \partial_j v_i. \quad (\text{A.6})$$

Then, inserting Eqs. (A.5) and (A.6) in Eq. (A.4), we obtain

$$\begin{aligned} \frac{d \cos \theta}{dt} &= -\frac{\partial_i P}{\rho (v_k v_k)^{1/2}} (b_i - u_i \cos \theta) \\ &\quad + b_j \partial_j v_i (u_i - b_i \cos \theta) - \left[\frac{B_j \partial_j B_i - B_j \partial_i B_j}{\rho (v_k v_k)^{1/2}} \right] u_i \cos \theta, \end{aligned} \quad (\text{A.7})$$

which can be rearranged as

$$\begin{aligned} \frac{d \cos \theta}{dt} &= \left[-\frac{\partial_i P}{\rho v} + \left(\frac{B_j \partial_j B_i - B_j \partial_i B_j}{\rho v} \right) + \partial_i v \right] (b_i - u_i \cos \theta) \\ &\quad + \frac{1}{2} (\partial_j v_i + \partial_i v_j) [u_i u_j - b_i b_j] \cos \theta, \end{aligned} \quad (\text{A.8})$$

where $v \equiv (v_k v_k)^{1/2}$.

If $\cos \theta = \pm 1$, that is to say $b_i = \pm v_i$, Eq. (A.8) implies that $d \cos \theta / dt = 0$, as its third term vanishes because it corresponds to the Lorenz force times the velocity, which is proportional to \mathbf{B} . This implies that alignment between \mathbf{B} and \mathbf{v} is expected since $\cos \theta = \pm 1$ constitutes an equilibrium point, as in the case of the relative orientation between $\nabla \rho$ and \mathbf{B} . However, unlike Eq. (13),

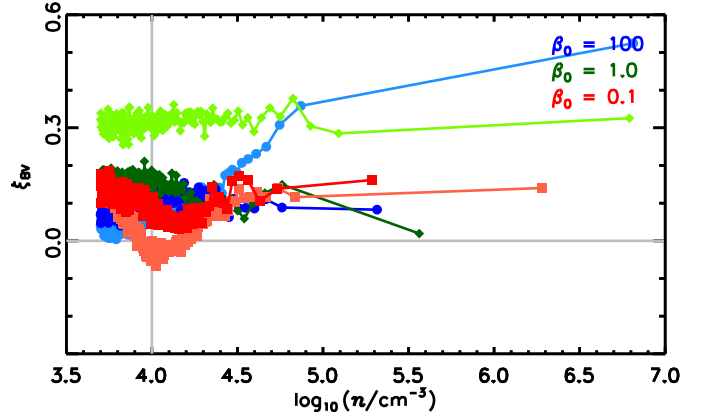


Fig. A.1. Relative orientation parameter, ξ_{BV} , as a function of particle density, $n \equiv \rho/\mu$, in the simulations used in Soler et al. (2013). The values of ξ_{BV} correspond to the relative orientation between \mathbf{B} and \mathbf{v} in n -bins with an equal number of voxels, all with $n > 500 \text{ cm}^{-3}$. The values $\xi_{\text{BV}} > 0$ correspond to \mathbf{B} mostly perpendicular to \mathbf{v} and $\xi_{\text{BV}} < 0$ correspond to \mathbf{B} mostly parallel to \mathbf{v} . The gray horizontal line is $\xi_{\text{BV}} = 0$, which corresponds to the case where there is no preferred relative orientation between \mathbf{B} and \mathbf{v} . The colors and the symbols represent the initial magnetization values quantified by β_0 . The darker colors represent the early snapshots in the simulation and the lighter colors represent the later snapshots. The gray vertical line, drawn for reference, corresponds to $n = 10^4 \text{ cm}^{-3}$.

the configuration $\cos \theta = 0$ is not an equilibrium point due to the first term on the right-hand side of Eq. (A.8), which account for the forces.

The predominant alignment between \mathbf{B} and \mathbf{v} was previously reported in Boldyrev (2006), Matthaeus et al. (2008), and Banerjee et al. (2009), and more recently studied in the context of MC formation in Iffrig & Hennebelle (2017). However, Eq. (A.8) constitutes a novel general expression that links the relative orientation between the two vectors. It relates the relative orientation to the underlying physical conditions, which is potentially useful in the interpretation of observations such as those of the magnetically aligned velocity anisotropy reported in Heyer et al. (2008, 2016) and the correlations between the $\langle \hat{\mathbf{B}}_{\perp} \rangle$ and the line-of-sight velocity gradients reported in Yuen & Lazarian (2017). Additionally, it provides reference to the assumptions behind methods for the estimation of the magnetic field strength, such as those presented in Houde et al. (2009) and González-Casanova & Lazarian (2017).

For the sake of illustration, we present the analysis of the relative orientation between \mathbf{B} and \mathbf{v} in the Soler et al. (2013) simulations in Fig. A.1. There we show that in the range $n > 500 \text{ cm}^{-3}$, the alignment between \mathbf{B} and \mathbf{v} is prevalent under the physical conditions included in those simulations, although the trends for increasing density are not as uniform as in the case of $\nabla \rho$ and \mathbf{B} . These trends are different in the first and the second snapshot as a consequence of the decay of the turbulence: stronger shocks tend to shift the alignment of \mathbf{B} and \mathbf{v} , as the transverse component of the magnetic field is amplified and the velocity tends to be perpendicular to it (Passot et al. 1995).